

# General and efficient simulation of pulse EPR spectra†

Stefan Stoll\* and R. David Britt

Received 14th April 2009, Accepted 3rd June 2009

First published as an Advance Article on the web 2nd July 2009

DOI: 10.1039/b907277b

We present a rather general and efficient method of simulating electron-spin echo spectra for spin systems where the microwave frequency does not simultaneously excite EPR transitions that share a common level. The approach can handle arbitrary pulse sequences with microwave pulses of arbitrary length and strength. The signal is computed as a sum over signals from the electron coherence transfer pathways contributing to the detected echo. For each pathway, amplitudes and frequencies of the signal components are computed and used to construct a spectral histogram from which the time-domain signal is obtained. For multinuclear spin systems, the nuclear subspace is factorized to accelerate the computation. The method is also applicable to high electron spin systems with significant zero-field splitting and to pulse electron-nuclear double resonance experiments. The method is implemented in the software package *EasySpin*, and several illustrative calculations are shown.

## 1. Introduction

Pulse electron paramagnetic resonance (EPR) spectroscopy is a powerful technique that reveals otherwise inaccessible details about the electronic and geometric structure of paramagnetic centers and their nanoscale environments in a large range of system of interest in biology, chemistry, physics and material sciences.<sup>1–4</sup> It can resolve weak interactions between electron spins and between electron and nuclear spins that cannot be resolved with continuous-wave (cw) EPR. The extraction of structural information from pulse EPR spectra is a two-step process: first, the parameters of the underlying spin Hamiltonian model are determined from the experimental spectra. Then, an analysis of these spectroscopic parameters reveals information about the electronic and the geometric structure. Numerical simulation plays a central role in this process, as complete extraction of the spectroscopic parameters from the spectra is generally not possible without it.

The utility of pulse EPR spectra therefore depends directly on the quality and the power of available numerical simulation techniques. Whereas such methods are well established in cw EPR<sup>5–8</sup> and validated against experiment, current pulse EPR simulation methodology is more limited in its capabilities and not as extensively tested. Currently available approaches based on analytical scalar formulas work well in some situations, but are often limited to one or a few specific experiments and to special cases such as a single nucleus, axial hyperfine tensors, no (or very small) nuclear quadrupole coupling, an isotropic  $g$  tensor, or infinitely short (ideal) pulses. High-electron spin systems are rarely supported, and programs are mostly restricted to one or two nuclei, even though it is often necessary to include many nuclei in the simulation.<sup>9,10</sup> For experiments where explicit scalar formulas

are not available, slow and inefficient simulations based on the general density matrix formalism are used, and a separate program has to be written from scratch for every new pulse EPR experiment. Substantial progress has been made in recent years,<sup>11–17</sup> but a general and efficient way to simulate pulse EPR spectra is still desirable.

In order to overcome these limitations in applicability, scope and performance, we have derived and implemented a reasonably general method that enables the numerical simulation of spectra from many pulse EPR and pulse electron-nuclear double resonance (ENDOR) experiments where electron-spin echoes are detected, without the need to manually derive explicit analytical expressions in advance. The method is based on density matrix dynamics as previously applied to specific experiments,<sup>1,18–26</sup> but is independent of a specific pulse sequence and avoids many time-consuming operations by pre-analyzing the experiment in terms of coherence transfer pathways and computing only those pathways that are actually detected in the experiment. Also, it uses a variation<sup>27</sup> of the frequency-domain histogram technique<sup>12,21,28–31</sup> rather than the simpler, but much slower time-domain evolution<sup>11,13,14</sup> in order to reduce the usually long computation times for powder samples and multinuclear spin systems. The method presented here is implemented in *EasySpin*,<sup>7,8</sup> a widely used software for cw EPR and ENDOR simulations, where it is integrated with local, global and hybrid least-squares fitting methods.

The article is structured as follows: initially, we summarize the fundamentals of the density matrix treatment for pulse EPR experiments and outline the theoretical essence of our approach based on nuclear sub-Hamiltonians, individual electron coherence transfer pathways, and the construction of the time-domain signal *via* a frequency-domain filter technique. We discuss our method for ideal and non-ideal microwave pulses, introduce a new general subspace factorization formula (product rule) for multinuclear spin systems, and detail the extension to high electron spin systems and pulse ENDOR. After this, we present a few exemplary simulations of pulse

Department of Chemistry, University of California, Davis One Shields Ave, Davis, CA 95616, US. E-mail: sstoll@ucdavis.edu

† Dedicated to Arthur Schweiger (1946–2006).

EPR spectra. At the end, we summarize the salient features of our approach that set it apart from others and mention its limitations and possible future extensions.

## 2. Basics of the theory

### General Hamiltonian

The spin Hamiltonian for a spin system with an electron spin with arbitrary  $S$  and a number of nuclear spins is

$$H_0 = H_S + \sum_k [SA_k I_k - \gamma_{n,k} B_0 I_k + I_k P_k I_k], \quad (1)$$

where the sum runs over all those nuclei with small hyperfine couplings that are observed with ESEEM or pulse ENDOR, and  $H_S$  collects the interactions of the electron spin (electron Zeeman interaction, zero-field tensors) and all nuclei with large hyperfine couplings that are not observed directly in the pulse EPR experiments, but affect the resonance fields of EPR transitions. The corresponding energy levels are illustrated in Fig. 1. The Hamiltonian is in angular frequency units, and all the symbols have their usual meanings. The first term in the sum is the hyperfine interaction, the second is the nuclear Zeeman interaction, and the third is the nuclear quadrupole interaction. The specific form of  $H_S$  is not relevant for our purposes, and we only assume that its energy levels are spaced such that microwave pulses cannot simultaneously excite transitions that share a common level. For the moment, we will restrict ourselves to one electron spin and a single ESEEM nucleus. Extensions to electron spins with  $S > 1/2$  and to more than one nuclei are discussed later.

During a microwave pulse of angular frequency  $\omega_{mw}$  and phase  $\phi$ , an additional term

$$H_1 = 2(\mu_B/\hbar) \mathbf{B}_1 g \mathbf{S} \cos(\omega_{mw} t + \phi) \quad (2)$$

is present in the Hamiltonian, where  $2\mathbf{B}_1$  is the magnetic field component of the microwave and is perpendicular to  $\mathbf{B}_0$ . For an anisotropic  $g$  tensor, this results in two oscillating components acting upon  $S$ , one perpendicular to  $\mathbf{B}_0$  and one parallel to it. We will neglect the latter one,<sup>1</sup> as it modulates the energy levels on a time scale much faster than the pulse EPR experiment.

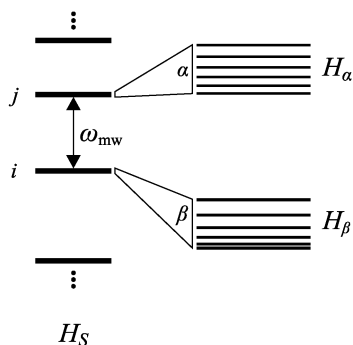


**Fig. 1** Energy level diagram for the type of spin systems addressed in this paper. Each level of  $H_S$  is split into a manifold of nuclear sublevels due to nuclei with small hyperfine couplings that are observed in the pulse EPR experiment.  $\omega_{mw}$  is the microwave frequency.

### Sub-Hamiltonians

A nucleus observed in ESEEM and pulse ENDOR usually interacts only weakly with the electron spin in the system, that is, the energy levels of  $H_S$  are barely affected by the small additional local field due to the hyperfine coupling with the nuclear magnetic moment. The electron spin precesses much faster than the nuclear spin, and thus the nucleus feels only the time-average effect of the electron spin vector  $\mathbf{S}$ , which is different for each eigenstate  $|i\rangle$  of  $H_S$ . Therefore, we can replace the operator  $\mathbf{S}$  in the hyperfine interaction terms in eqn (1) with the expectation value  $\langle i|\mathbf{S}|i\rangle$  and write a separate nuclear sub-Hamiltonian for each electron spin manifold  $i$ , in angular frequency units,

$$H_i = \langle i|\mathbf{S}|i\rangle A I - \gamma_n B_0 I + I P I. \quad (3)$$

For the simplest case of a single unpaired electron ( $S = 1/2$ ),  $H_S$  describes a two-level system and  $i$  corresponds to  $m_S$ , taking the values  $+1/2$  and  $-1/2$  for the higher and lower energy eigenstate, respectively.

The nuclear sub-Hamiltonians  $H_i$  are  $(2I + 1) \times (2I + 1)$  matrices usually represented in the nuclear Zeeman basis  $|m_I\rangle$  ( $m_I = -I, \dots, I$ ) and can be diagonalized by the transformation

$$H_i^{\text{diag}} = \varepsilon^{(i)} = M_i^\dagger H_i M_i, \quad (4)$$

where  $\varepsilon^{(i)}$  is a diagonal matrix with the eigenvalues (energies) of  $H_i$  on the diagonal and  $M_i$  is a unitary matrix with the eigenvectors (stationary states) of  $H_i$  as columns.

If the nuclear quadrupole interaction is zero,  $M_i$  can be computed analytically. The nuclear spin coordinate system can be chosen such that all  $I_y$  terms in  $H_i$  vanish.  $M_i$  then assumes the simple form  $M_i = \exp(i\eta_i I_y)$ , where  $\eta_i = \arccos(\mathbf{z} \cdot \mathbf{z}_{\text{eff},i})$  is the angle between the external magnetic field direction and the nuclear spin quantization axis for the given manifold. When represented in the Zeeman basis,  $M_i$  turns out to be real and symmetric with respect to its antidiagonal. In angular momentum context, it is equal to the Wigner rotation matrix  $\mathcal{D}^I(0, \eta_i, 0) = d^I(\eta_i)$  for angular momentum  $I$ . The nuclear Hamiltonian in its eigenbasis now reads  $\omega_i I_z$ , with  $\omega_i = |\langle i|\mathbf{S}|i\rangle A - \gamma_n B_0|$ . So  $m_I$  is a “good” quantum number, and the nuclear sublevels are equally spaced within each manifold. When the nuclear quadrupole is not zero, eigenvalues and eigenvectors are not simple anymore and are best obtained by numerical diagonalization.<sup>29,32</sup> There do exist analytical solutions for the eigenvalues and eigenstates of  $I = 1$  and  $I = 3/2$  nuclei,<sup>33,34</sup> but due to their complexity they are of limited utility. For  $I = 1$  nuclei ( $^2\text{H}$ ,  $^{14}\text{N}$ , and  $^6\text{Li}$ ), an elegant graphical method has been devised that helps to determine the eigenvalue of  $H_i$ .<sup>35,36</sup> In this work, we do not place any restrictions on the size of the nuclear quadrupole interaction.

### Dynamics

The state of an ensemble of spin systems is described by a density matrix  $\sigma$  that changes with time  $t$  according to

$$\sigma(t) = U(t)\sigma(0)U(t)^\dagger, \quad (5)$$

where  $\sigma(0)$  is the initial density matrix, and  $U(t)$  is the unitary propagator matrix determined by the Schrödinger equation

$\dot{U} = -iH(t)U(t)$  with  $U(0) = \mathbb{1}$ . If the Hamiltonian  $H$  is time-independent, then this gives a closed exponential form for the propagator,

$$U(t) = e^{-iHt}, \quad (6)$$

otherwise  $U(t)$  has to be obtained by numerical integration. The propagator  $U$  assumes different forms during a microwave pulse and during free evolution, as the Hamiltonians governing these two periods are different.

At the beginning of the experiment, all spin systems are in thermal equilibrium. The thermal equilibrium density matrix  $\sigma_{\text{eq}}$  is given by the Boltzmann distribution

$$\sigma_0 = \sigma_{\text{eq}} = \beta / \text{tr } \beta \text{ with } \beta = e^{-\hbar H/k_{\text{B}}T}. \quad (7)$$

$\sigma_{\text{eq}}$  is diagonal in the complete eigenbasis of the spin Hamiltonian, and its diagonal elements represent the fractional populations of the energy levels at thermal equilibrium. Since  $H_S$  dominates,  $H \approx H_S$ , the  $N$  nuclear sublevels of each manifold  $i$  all have essentially identical fractional populations of  $p_i/N$ , with a total manifold fractional population of  $p_i$ .

We do not place any restrictions such as the high-field approximation on the computation of  $p_i$  for  $H_S$  from eqn (7). Also, there are experimental situations in which the ensemble is not at thermal equilibrium at the beginning of a pulse sequence. If the repetition rate is very high, the out-of-equilibrium state after the previous pulse sequence might not have relaxed back to  $\sigma_{\text{eq}}$ . This can be the case for pulse ENDOR spectra obtained with high repetition rates at high fields and low temperatures (e.g. 95 GHz below about 5 K).<sup>37–39</sup> Another case is when the paramagnetic center is generated in the experiment in a spin-polarized state. These situations can be accommodated by computing appropriate non-equilibrium  $p_i$  for the energy levels of  $H_S$ .

Finally, to obtain the quadrature signal  $E$  of the echo amplitude from the density matrix, the expectation value of  $S_+ = S_x + iS_y$  is computed,

$$E = \langle S_+ \rangle = \text{tr} (S_+ \sigma). \quad (8)$$

Often only one signal phase is of interest. In that case, the signal is  $\langle S_x \rangle = \text{Re}\langle S_+ \rangle$ .

### 3. Submatrices and pathways

The theory outlined so far is very general, but for most common cases in pulse EPR it is not necessary to perform the computations in the full spin state space. Very often, the energy levels in  $H_S$  are such that it is not possible for microwave pulses to simultaneously excite two adjacent EPR transitions that share a common level. Then each pair of levels of  $H_S$  that is resonant with the microwave frequency can be treated as a separate two-level system of a fictitious electron spin  $S = 1/2$ . Each level is split into a manifold of nuclear sublevels. We denote the two manifolds with  $\alpha$  (higher energy) and  $\beta$  (lower energy), as illustrated in Fig. 1.

#### 3.1. Basic equations

For such a system, the spin Hamiltonian transformed to the “rotating” frame<sup>15</sup> and written in submatrix form is

$$H_0 = \begin{pmatrix} H_\alpha + \Omega_S/2 & 0 \\ 0 & H_\beta - \Omega_S/2 \end{pmatrix}. \quad (9)$$

$\Omega_S = \omega_S - \omega_{\text{mw}}$  is a resonance frequency offset that accounts for the fact that in an EPR sample the transition frequencies  $\omega_S$  are not all equal, but distributed over a range. This inhomogeneity can be due to different orientations of the individual spin systems in the spectrometer, to distributions in magnetic parameters such as tensor principal values or orientations, or to unresolved hyperfine splittings.

During microwave irradiation of strength  $\omega_1 = (\mu_{\text{B}}/\hbar)g|\mathbf{B}_1|$  and phase  $\phi$ , the additional term in the rotating frame Hamiltonian for the two-level system is

$$H_1 = \omega_1(S_x \cos \phi + S_y \sin \phi). \quad (10)$$

$\phi = 0$  is denoted as  $x$  phase and  $\phi = \pi/2$  as  $y$  phase.

The nuclear sub-Hamiltonians of the two manifolds connected by the microwave resonant with the transition have different eigenvalues  $\varepsilon^{(\alpha)}$ ,  $\varepsilon^{(\beta)}$  and eigenstates  $M_\alpha$ ,  $M_\beta$ . The matrix

$$M = M_\alpha^\dagger M_\beta, \quad (11)$$

sometimes called the Mims matrix,<sup>40</sup> plays a central role in the theory of ESEEM.<sup>21,22,28</sup> It is the unitary overlap matrix between the nuclear eigenstates of the  $\alpha$  and those of the  $\beta$  manifold. If  $M$  is equal to the identity matrix  $\mathbb{1}$  (or a row or column permutation of it), each nuclear state in the  $\alpha$  manifold is identical to one in the  $\beta$  manifold. Consequently, there is no branching,<sup>21</sup> and there are no nuclear modulation effects. When all elements of  $M$  are nonzero, an  $\alpha$  nuclear state is a superposition of  $\beta$  nuclear states, and the microwave induces nuclear modulation effects.

**Dynamics.** The density matrix for an ensemble of two-level systems can be written as a block matrix with four components

$$\sigma = \begin{pmatrix} \sigma_\alpha & \sigma_+ \\ \sigma_- & \sigma_\beta \end{pmatrix}, \quad (12)$$

where  $\sigma_\alpha$ ,  $\sigma_\beta$ ,  $\sigma_+$  and  $\sigma_-$  are submatrices defined over the nuclear subspaces.  $\sigma_\alpha$  and  $\sigma_\beta$  represent all nuclear population and coherence components within the upper and the lower manifold, respectively, with electron coherence order 0, whereas the elements in  $\sigma_+$  and  $\sigma_-$  have electron coherence order  $+1$  and  $-1$ , respectively.<sup>25,41</sup>

When looking at an isolated pair of levels from  $H_S$  with  $N$  nuclear sublevels each, the start density matrix can be written as  $\sigma_{\text{eq}} = (p_\alpha S_\alpha + p_\beta S_\beta)/N$ , or

$$\sigma_{\text{eq}} = \frac{1}{N} \left( \frac{p_\alpha + p_\beta}{2} \mathbb{1} - \Delta p S_z \right) = \frac{1}{N} (p_\alpha \mathbb{1} + \Delta p S_\beta) \quad (13)$$

with the population difference  $\Delta p = p_\beta - p_\alpha$ . We have used  $\mathbb{1} = S_\alpha + S_\beta$  and  $2S_z = S_\alpha - S_\beta$ . The terms proportional to  $\mathbb{1}$  can be dropped without affecting the expectation values of the traceless operators  $S_+$  or  $S_x$  in eqn (8). For our purposes it is

advantageous to work with the last expression in eqn (13), containing  $S_\beta$ . The resulting effective density is

$$\sigma_{\text{eq}} = \frac{\Delta p}{N} S_\beta = \frac{\Delta p}{N} \begin{pmatrix} 0 & 0 \\ 0 & \mathbb{1} \end{pmatrix}, \quad (14)$$

different from the usual  $\sigma_{\text{eq}} = -(\Delta p/N)S_z$ , which is the conventional form of  $\sigma_{\text{eq}}$  adequate for computations using the product operator formalism with  $S_x$ ,  $S_y$  and  $S_z$ .<sup>1</sup> Our choice halves the number of non-zero elements in  $\sigma_{\text{eq}}$  and correspondingly reduces the computational effort. Also, it is physically intuitive, as it represents a state where all  $\beta$  sublevels are equally populated and all  $\alpha$  sublevels are empty. It is important to retain the prefactor in eqn (14).  $\Delta p$  is relevant for cases where  $H_S$  has more than two levels, as it may vary from transition to transition, and  $1/N$  is important for multinuclear systems, as this allows comparison of ESEEM signals from systems with different numbers of nuclei.

For computing the detected signal in eqn (8) at the submatrix level, we obtain

$$E = \text{tr}(\sigma_-) \quad E = \text{tr}(M\sigma_-). \quad (15)$$

in the nuclear Zeeman basis and nuclear eigenbasis, respectively.

Spelled out into the four submatrix components, a general propagator is of the form

$$U = \begin{pmatrix} U_\alpha & U_+ \\ U_- & U_\beta \end{pmatrix}. \quad (16)$$

The submatrices  $U_\alpha$  etc. are neither unitary nor Hermitian. Inserting eqn (12) and (16) into eqn (5), the propagation of the four density submatrices can be written as

$$\begin{pmatrix} \sigma_\alpha(t) \\ \sigma_\beta(t) \\ \sigma_+(t) \\ \sigma_-(t) \end{pmatrix} = \begin{pmatrix} \alpha|\alpha & +|+ & \alpha|+ & +|\alpha \\ -|- & \beta|\beta & -|\beta & \beta|- \\ \alpha|- & +|\beta & \alpha|\beta & +|- \\ -|\alpha & \beta|+ & -|+ & \beta|\alpha \end{pmatrix} \begin{pmatrix} \sigma_\alpha(0) \\ \sigma_\beta(0) \\ \sigma_+(0) \\ \sigma_-(0) \end{pmatrix} \quad (17)$$

where the shorthand  $+|\alpha$  indicates pre-multiplication with  $U_+$  and post-multiplication with  $U_\alpha^\dagger$ , etc.

**Free evolution.** The general propagator in the above equation can be simplified for the limiting case of free evolution. Then, the propagator is block-diagonal in the nuclear Zeeman basis

$$U_{\text{free}}(t) = e^{-iH_0 t} = \begin{pmatrix} A_t \phi_t & 0 \\ 0 & B_t \phi_t^* \end{pmatrix} \quad (18)$$

with the offset phase  $\phi_t = \exp(-i\Omega_S t/2)$  and the nuclear subpropagator matrices  $A_t$  and  $B_t$ . These can be diagonalized

$$A_t = e^{-iH_\alpha t} = M_\alpha e^{-i\epsilon_\alpha t} M_\alpha^\dagger = M_\alpha a_t M_\alpha^\dagger \quad (19a)$$

$$B_t = e^{-iH_\beta t} = M_\beta e^{-i\epsilon_\beta t} M_\beta^\dagger = M_\beta b_t M_\beta^\dagger, \quad (19b)$$

so that  $U_{\text{free}}$  is completely diagonal in the nuclear eigenbasis

$$U_{\text{free}}(t) = \begin{pmatrix} a_t \phi_t & 0 \\ 0 & b_t \phi_t^* \end{pmatrix}. \quad (20)$$

Consequently, the components of the density matrix change in time according to

$$\begin{aligned} \sigma_\alpha(t) &= a_t \sigma_\alpha a_t^\dagger \\ \sigma_\beta(t) &= b_t \sigma_\beta b_t^\dagger \\ \sigma_+(t) &= a_t \sigma_+ b_t^\dagger \phi_t^2 \\ \sigma_-(t) &= b_t \sigma_- a_t^\dagger \phi_t^{*2} \end{aligned} \quad (21)$$

The four density submatrices evolve separately, and only  $\sigma_+$  and  $\sigma_-$  acquire phase due to the resonance frequency offset.

**Pulses.** The propagator for a general microwave pulse of duration  $t_p$  is

$$P = e^{-i(H_0 + H_1)t_p} = \begin{pmatrix} P_\alpha & P_+ \\ P_- & P_\beta \end{pmatrix}. \quad (22)$$

In general, the four components of this propagator cannot be computed analytically and must be obtained by numerically calculating the full matrix exponential. However, often pulses are short and strong compared to the interaction strengths of the spin Hamiltonian, so that  $H_0$  in eqn (22) can be neglected. For these so-called ideal or hard pulses, the pulse propagator can be computed explicitly. With the flip angle  $\theta = \omega_1 t_p$ , and the abbreviations  $c = \cos(\theta/2)$ ,  $s = \sin(\theta/2)$  and  $k = e^{+i\phi}$ , it is

$$P_\phi(\theta) = e^{-i\theta(S_x \cos \phi + S_y \sin \phi)} = \begin{pmatrix} c\mathbb{1} & -isk^*\mathbb{1} \\ -isk\mathbb{1} & c\mathbb{1} \end{pmatrix} \quad (23)$$

in the nuclear Zeeman basis, or

$$P_\phi(\theta) = \begin{pmatrix} c\mathbb{1} & -isk^*M \\ -iskM^\dagger & c\mathbb{1} \end{pmatrix} \quad (24)$$

in the nuclear eigenbasis. The presence of the matrix  $M$  in eqn (24) indicates that the nuclear coherences and polarizations get shuffled within each submatrix as a result of a pulse. If the pulses have  $y$  phase ( $\phi = 90^\circ$ ), the propagator becomes

$$P_y(\theta) = \begin{pmatrix} c\mathbb{1} & -s\mathbb{1} \\ s\mathbb{1} & c\mathbb{1} \end{pmatrix} \quad P_y(\theta) = \begin{pmatrix} c\mathbb{1} & -sM \\ sM^\dagger & c\mathbb{1} \end{pmatrix}, \quad (25)$$

again in the nuclear Zeeman and eigenbasis, respectively. Two very common special cases are ideal pulses with flip angles of  $\theta = 90^\circ$  and  $\theta = 180^\circ$

$$P_y(90^\circ) = \frac{1}{\sqrt{2}} \begin{pmatrix} \mathbb{1} & -M \\ M^\dagger & \mathbb{1} \end{pmatrix} \quad (26)$$

$$P_y(180^\circ) = \begin{pmatrix} 0 & -M \\ M^\dagger & 0 \end{pmatrix}.$$

Inserting these expression into eqn (17), one can see that an ideal  $90^\circ$  pulse transfers magnetization from each of the four subcomponents of the density matrix to all others. An ideal  $180^\circ$  only transfers  $\alpha$  to/from  $\beta$  as well as  $+$  to/from  $-$ .

**Transfer pathways.** In general, therefore, a microwave pulse transfers magnetization from any of the four density submatrices to any other. During free evolution, magnetization evolves within these submatrices and acquires an offset phase, but is not transferred between levels or sublevels. Before the

first pulse, the magnetization is in  $\beta$  only. The first pulse transfers and distributes this magnetization to all four components  $\alpha$ ,  $\beta$ ,  $+$  and  $-$ , and after the pulse the four parts of the magnetization evolve separately and independently. The next pulse distributes the magnetization further, so that there are now 16 different components,  $\beta \rightarrow \alpha \rightarrow \alpha$ ,  $\beta \rightarrow \alpha \rightarrow \beta$ ,  $\beta \rightarrow \alpha \rightarrow +$  etc. We abbreviate these transfer pathways as  $(\alpha\alpha)$ ,  $(\alpha\beta)$ ,  $(\alpha+)$  etc., dropping the  $\beta$  from the initial equilibrium state, as it is the same for all pathways. At the end of the pulse sequence the density matrix is a sum of matrices describing independent magnetization components that evolved along different transfer pathways  $q$

$$\sigma = \sum_q \sigma^{(q)}. \quad (27)$$

This concept of pathways is useful in developing phase cycles for pulse EPR experiments.<sup>25,41</sup> Phase cycling amounts to selecting specific pathways, which can be done directly in a simulation. Along each pathway, spins acquire distinct phases. They acquire offset phase only when evolving as  $+$  or  $-$  electron coherence. An echo is formed whenever spins with different offset frequencies have simultaneously zero phase and refocus. This happens when the spins have spent equal times in  $+$  and in  $-$ . Thus, only these pathways contribute to the echo. Also, according to eqn (15), only pathways ending in  $-$  are observable. From the actual values of the inter-pulse delays and dwell times for a pulse experiment, it is therefore straightforward to identify all pathways that result in an observable echo at the detection point,<sup>41</sup> independent of the values of the incremented delays. Usually, this is only a small fraction of all pathways.

Sometimes, the actual experiment excludes some of these refocusing pathways by phase cycling or by the mere fact that magnetization along them disappears due to relaxation. This can be accommodated very easily by excluding pathways from the list that do not feature the correct coherence order during the various inter-pulse delays. For example, in the one-dimensional four-pulse sum combination peak experiment<sup>42,43</sup>  $(90^\circ)_{y-\tau}-(90^\circ)_{y-T}-(180^\circ)_{y-T}-(90^\circ)_{y-\tau}$ -(echo) $_x$  the pathways  $(+\alpha\beta-)$  and  $(+ + - -)$  in theory contribute equally to the echo, among others. The latter is usually negligible due to transverse relaxation, or phase cycled out. In a simulation, it can be removed by requiring that all pathways included in the simulation have zero electron coherence order ( $\alpha$  or  $\beta$ ) during the second free evolution period. This pathway (and echo) selection is one of the major advantages of the submatrix formalism over full-space simulations,<sup>13,14,16</sup> where the effect of phase cycling and pathway selection can only be accommodated by explicit zeroing of density matrix elements or by explicitly simulating all steps of the phase cycle.

Once all contributing pathways are determined, the signal of each of these pathways is computed in turn. The total signal is the sum of the individual pathway signals, as the density is the sum of contributions from all pathways, in the nuclear eigenbasis

$$E = \text{tr} \left( M \sum_q \sigma^{(q)} \right) = \sum_q \text{tr} \left( M \sigma^{(q)} \right) = \sum_q E^{(q)}. \quad (28)$$

### 3.2 Algorithm

The eqn (14), (17), (20), (24) and (28) are all the quantum mechanical ingredients necessary to compute the measured signal of an electron-spin echo experiment. With these equations, it is easy to write a simple computer program that quickly computes the signal for any arbitrary pulse sequence by constructing explicit submatrix expressions. The algorithm works as follows.

First, as outlined above, the pulse sequence (defined by the number of microwave pulses and their flip angles), the initial interpulse delays and the incrementation scheme (defining which delays are kept constant and which ones are incremented or decremented along which dimension) are examined to determine which pathways refocus at the detection point and hence contribute to the echo of interest.<sup>41</sup> Next, for each of the pathways, a list of propagator submatrices constituting the product representing the density at the detection point is constructed. In this product, adjacent factors not containing incremented delays are multiplied together, whereas propagator submatrices that contain varied delays are kept separate.<sup>13</sup> The resulting expression can be expanded at the scalar level and is used to construct the spectrum. We illustrate these first steps leading to the scalar expression for two common ESEEM experiments, suppressing the  $\Delta p/N$  prefactor from eqn (14) temporarily, to unclutter the notation.

The two-pulse ESEEM experiment uses the sequence  $(90^\circ)_{y-\tau}-(180^\circ)_{y-\tau}$ -(echo) $_x$ , with the echo amplitude measured as a function of  $\tau$ . The only pathway generating the echo is  $(+ -)$ , i.e.  $\beta \rightarrow + \rightarrow -$ . Using eqn (18), (20) and (26), the trace expression for the corresponding signal is

$$E^{(+ -)} = \frac{1}{2} \text{tr}(B_\tau A_\tau B_\tau^\dagger A_\tau^\dagger) = \frac{1}{2} \text{tr}(M b_\tau M^\dagger a_\tau M b_\tau^\dagger M^\dagger a_\tau^\dagger). \quad (29)$$

in the Zeeman and in the eigenbasis, respectively. The prefactor 1/2 stems from the  $\beta \rightarrow +$  transfer amplitude of the  $90^\circ$  pulse. Expanding all matrices and the trace, we get the scalar expression

$$E^{(+ -)} = \frac{1}{2} \sum_{ijkl} (M_{ij}^\dagger M_{jk} M_{kl}^\dagger M_{li}) \cdot e^{-i(\omega_{jk}^\beta + \omega_{jl}^\alpha)\tau}, \quad (30)$$

where  $\omega_{ij} = \varepsilon_i - \varepsilon_j$ .

The HYSORE experiment is based on the sequence  $(90^\circ)_{y-\tau}-(90^\circ)_{y-t_1}-(180^\circ)_{y-t_2}-(90^\circ)_{y-\tau}$ -(echo) $_x$ , where  $t_1$  and  $t_2$  are varied independently. The pathways contributing to the echo are  $(+\alpha\beta-)$  and  $(+\beta\alpha-)$ , giving  $\alpha/\beta$  and  $\beta/\alpha$  cross peaks in the two-dimensional spectrum, respectively. Each pathway signal is given by the trace of a product of evolution matrices

$$E^{(+\alpha\beta-)} = -\frac{1}{8} \text{tr}(B_\tau B_{t_2} A_{t_1} A_\tau B_\tau^\dagger A_{t_1}^\dagger B_{t_2}^\dagger A_\tau^\dagger) \quad (31a)$$

$$E^{(+\beta\alpha-)} = -\frac{1}{8} \text{tr}(B_\tau A_{t_2} B_{t_1} A_\tau B_\tau^\dagger B_{t_1}^\dagger A_{t_2}^\dagger A_\tau^\dagger) \quad (31b)$$

in the nuclear high-field basis, or

$$E^{(+\alpha\beta-)} = -\frac{1}{8} \text{tr}(Mb_{\tau}b_{t_2}M^{\dagger}a_{t_1}a_{\tau}Mb_{\tau}^{\dagger}M^{\dagger}a_{t_1}^{\dagger}Mb_{t_2}^{\dagger}M^{\dagger}a_{\tau}^{\dagger}) \quad (32a)$$

$$E^{(+\beta\alpha-)} = -\frac{1}{8} \text{tr}(Mb_{\tau}M^{\dagger}a_{t_2}Mb_{t_1}M^{\dagger}a_{\tau}Mb_{\tau}^{\dagger}b_{t_1}^{\dagger}M^{\dagger}a_{t_2}^{\dagger}a_{\tau}^{\dagger}) \quad (32b)$$

in the nuclear eigenbasis. The total signal is the sum of these two pathway signals. The prefactor  $-1/8$  stems from the electron spin transfer amplitudes of the four pulses. If all terms independent of  $t_1$  and  $t_2$  are grouped, the signals can be written as

$$E^{(+\alpha\beta-)} = -\frac{1}{8} \text{tr}(b_{t_2}M^{\dagger}a_{t_1}G^{\alpha}a_{t_1}^{\dagger}Mb_{t_2}^{\dagger}D^{\beta}) \quad (33a)$$

$$E^{(+\beta\alpha-)} = -\frac{1}{8} \text{tr}(a_{t_2}Mb_{t_1}G^{\beta}b_{t_1}^{\dagger}M^{\dagger}a_{t_2}^{\dagger}D^{\alpha}) \quad (33b)$$

which in scalar form reads

$$E^{(+\alpha\beta-)} = -\frac{1}{8} \sum_{ijkl} (M_{ij}^{\dagger}G_{jk}^{\alpha}M_{kl}D_{li}^{\beta}) \cdot e^{-i\omega_{jk}^{\alpha}t_1} \cdot e^{-i\omega_{il}^{\beta}t_2} \quad (34a)$$

$$E^{(+\beta\alpha-)} = -\frac{1}{8} \sum_{ijkl} (M_{ij}G_{jk}^{\beta}M_{kl}^{\dagger}D_{li}^{\alpha}) \cdot e^{-i\omega_{jk}^{\beta}t_1} \cdot e^{-i\omega_{il}^{\alpha}t_2} \quad (34b)$$

$G$  contains the amplitudes of the nuclear coherences generated by the first two pulses, and  $D$  is the nuclear coherence detector efficiency of the part of the pulse sequence after the delay  $t_2$ .  $M$  and  $M^{\dagger}$  contain the transfer amplitudes from the  $t_1$  delay to the  $t_2$  delay.

For any one- (1D) or two-dimensional (2D) pulse experiment, even more unusual ones (*e.g.* the CF-NF experiment,<sup>44</sup> DONUT-HYSCORE,<sup>45</sup> or 2D refocused primary ESEEM,<sup>46</sup>) equivalents of eqn (30) and (34) can be generated by a program immediately from the information about the pulse experiment and the pathways. All the resulting expressions are sums over many different harmonic components, each with its own amplitude  $Z$  and frequency  $-\omega$

$$E^{(q)}(t) = c_q \sum_{\xi} Z_{\xi}^{(q)} \cdot e^{-i\omega_{\xi}^{(q)}t} \quad \text{or} \quad (35)$$

$$E^{(q)}(t_1, t_2) = c_q \sum_{\xi} Z_{\xi}^{(q)} \cdot e^{-i\omega_{\xi}^{(q)}t_1} \cdot e^{-i\omega_{2\xi}^{(q)}t_2}.$$

The amplitudes  $Z$  consist of products of matrix elements of generator, detector and transfer matrices. The time-dependent complex exponentials contain the nuclear frequencies (and possibly combinations thereof) during the various incremented time intervals.

**Spectrum construction.** Starting from an expression of the form given in eqn (35), there are two common ways to construct the echo modulation signal, as already noted by Mims.<sup>21</sup> One is to take amplitude and frequency of each component in turn and evaluate the exponential over the entire 1D or 2D time domain.<sup>11,13,14</sup> The other is to construct a frequency-domain stick spectrum (histogram) by accumulating the amplitudes into

a spectral array at the positions corresponding to the frequencies, then inverse Fourier transforming the histogram and discarding the points corresponding to negative times.<sup>12,21,28-31</sup>

Both methods have disadvantages. The time-domain method is slow, as it has to compute a complex-valued time-domain signal for every single component separately. This is specially time consuming for two-dimensional signals like HYSCORE and makes all but the most elementary simulations prohibitively slow. The frequency-domain method is extremely fast per component, but since a finite-size histogram is constructed, peak positions have to be rounded to the nearest bin of the histogram, leading to systematic errors in the final signal. To reduce the size and hence the impact of the rounding error, the resolution of the histogram can be increased and the time domain obtained after inverse Fourier transform is then truncated.<sup>12</sup> However, artifacts decrease very slowly with increasing histogram resolution. Especially in 2D spectra, rounding artifacts such as ragged powder ridges and incomplete phase cancelations can be visible even if the histogram is 16 times higher resolved than necessary for the final time domain signal. In the simulation of powder spectra, artifacts can be mitigated by substantially increasing the number of orientations at the cost of performance, but systematic errors can persist.

The disadvantages of both methods can be avoided by using a filter technique that works similar to the frequency-domain method, but uses a truncated continuous filter kernel function instead of a single delta function for binning the frequencies in a histogram fashion, thus avoiding any shifting of the peak from its correct position. Details of the filter method are described in ref. 27. As a result, powder ridges are smooth, and destructive phase interference in 2D spectra is correctly modeled. Compared to time-domain evolution, the method is as accurate and requires as few orientations, while being much faster. Compared to the histogram binning, the method is somewhat slower for each component, but requires a smaller frequency-domain array and saves time due to the smaller orientational resolution needed and, for 2D spectra, the faster inverse Fourier transformation.

**Powder integration.** In order to simulate the spectrum from a powder sample, signals have to be computed for and summed over all possible orientations of the spin system with respect to the external magnetic field. Depending on the number, symmetry and relative orientation of the interaction tensors, the integration domain extends over half the unit sphere, one or two octants, or just a quarter meridian. We use a simple triangular grid.<sup>5,7,47</sup> Nuclear transitions observed experimentally with ESEEM or pulse ENDOR are much less anisotropic than EPR transitions. Consequently, it is sufficient to use few orientations (typically steps between 0.25 and 1°). In contrast to cw EPR,<sup>7,47</sup> orientational interpolation does not seem to yield significant performance increases.

**Orientation selection.** If the eigenvalues of  $H_S$  are anisotropic, *e.g.* in the case of an anisotropic  $g$  tensor of a  $S = 1/2$ , a  $D$  tensor for  $S > 1/2$  or large hyperfine splittings from a strongly coupled nucleus, the microwave frequency will be resonant with transitions from  $H_S$  only for certain orientations of the

spin system with respect to the external magnetic field. This orientation and transition selectivity means that the echo signals have to be computed only for these few orientations. The magnetic parameters determining  $H_S$  are usually known from cw EPR spectra, so that the orientation and transition selectivity can be pre-computed independent of the magnetic parameters of the ESEEM or ENDOR nuclei. This results in substantial time savings in iterative automatic or manual fittings.

## 4. Extensions of the theory

The submatrix theory outlined above was developed assuming ideal pulses and two levels in  $H_S$ . It can easily be extended to non-ideal pulses and to high electron spin systems with more than two levels, as we describe in the following. Also, we discuss a factorization method for multinuclear spin systems that helps accelerate simulations, and we give details on how to compute pulse ENDOR spectra.

### 4.1. Non-ideal pulses

So far, we have assumed ideal pulses whose lengths  $t_p$  are so short that dynamics during the pulse other than the nutation of the spins can be neglected, and that the excitation bandwidth ( $\approx 1/t_p$ ) of the pulse is so large that all subtransitions in a pair of manifolds are flipped by the same angle  $\omega_1 t_p$ . In practice, however, the length of the microwave pulses is not always negligible. Indeed, pulses are often chosen to be long to be selective or semi-selective with respect to the subtransitions (as in Davies ENDOR<sup>48,49</sup>) or to allow for optimal coherence transfers during the pulse (such as in matched pulses<sup>50-52</sup>). This results in two effects: not all subtransitions are excited equally, and the spins not only nutate but have time to also evolve during the pulse. The static Hamiltonian during the pulse cannot be neglected, and the complete Hamiltonian  $H = H_0 + H_1$  must be used in the pulse propagator in eqn (22).

Such non-ideal pulses can be easily incorporated into the formalism described above. First, the full propagator  $P$  in eqn (22) is computed numerically for each pulse that cannot be approximated as ideal. Then, these propagators are used in the construction of the trace expressions for the echo amplitude. Since the pulse propagators depend on the frequency offset  $\Omega_S$ , the trace expressions have to be integrated over  $\Omega_S$ , weighed by an appropriate distribution function for the frequency offset.

As an example, we look again at the two-pulse ESEEM experiment, this time with pulses with arbitrary strength and duration, described by the propagators  $P_1$  and  $P_2$  in submatrix notation given in eqn (22). Similar to eqn (29), we can write directly

$$E^{(+)} = \text{tr}(M b_{\tau} P_{2-} a_{\tau} P_1 + P_{1\beta}^{\dagger} b_{\tau}^{\dagger} P_{2+}^{\dagger} a_{\tau}^{\dagger}). \quad (36)$$

The ideal-pulse expression in eqn (29) is a special case of this with  $P_{2-} = M^{\dagger}$ ,  $P_1 + P_{1\beta}^{\dagger} = M$ , and  $P_{2+}^{\dagger} = M^{\dagger}$ , and the prefactor of 1/2 resulting from the product of the transfer amplitudes of the ideal pulses (see eqn (26)). For other experiments, the trace expressions can be written down just as easily. Apart from the numerical computation of the pulse propagators and the integration over  $\Omega_S$ , the procedure of ideal and non-ideal pulses is identical.

In pulse sequences with ideal 180° pulses, the zero diagonal submatrices in eqn (26) meant that some pathways were not populated, even though the spins in these pathways would refocused at the detection point. This is not the case anymore with non-ideal pulses. *E.g.* in HYSORE the additional pathways ( $+\alpha\alpha-$ ) and ( $+\beta\beta-$ ) have to be included in the simulation,<sup>12</sup> although their amplitude will be smaller than the one of the two main ones ( $+\alpha\beta-$ ) and ( $+\beta\alpha-$ ).

Partial excitation by selective microwave pulses can be accounted for in two more approximate ways. Zhidomirov *et al.*<sup>19</sup> used sums of single-transition operators, and Keijzers *et al.*<sup>29</sup> used an explicit pulse excitation profile  $G$  and weighed the elements of  $M$  according to the resonance offset,  $M'_{ij} = M_{ij} G(\omega_{ij} - \omega_{mw})$ . Both methods, however, do not take evolution during the pulse into account.

### 4.2. High electron spin systems

The theory for pulse EPR of high electron spin systems has been developed over the years, for ESEEM of organic triplets,<sup>53-55</sup> as well as for ESEEM<sup>15,20,31,40,56,57</sup> and pulse ENDOR<sup>58-60</sup> of high-spin transition metal ions. An electron spin  $S > 1/2$  affects pulse EPR spectra in several ways. First, due to additional anisotropic zero-field interactions, the experiment becomes orientation- and transition-selective for a given microwave frequency and magnetic field, even if the  $g$  tensor is isotropic. Second, there are more than two manifolds and correspondingly more nuclear sub-Hamiltonians and nuclear frequencies. As discussed, these nuclear frequencies depend on the expectation value  $\langle S \rangle$  of each manifold. In the limit of small zero-field splitting where the nonsecular terms of the zero field splitting can be neglected, the electron spin is aligned along the external field direction  $z$  in all states,  $\langle m_S | S | m_S \rangle = m_S z$  and just has a  $m_S$ -dependent magnitude. In general, both the magnitude and the direction of  $\langle S \rangle$  will depend on the eigenstate of  $H_S$ . Third, the EPR transition moments for the different EPR transitions are different, so that a given microwave pulse results in nutation frequencies and flip angles that differ from transition to transition.

To take these effects into account,<sup>56</sup> the matrix elements of  $x \cdot S$  in the eigenbasis of  $H_S$  are computed, where  $x$  is the direction of the oscillating magnetic field component of the incident microwave. A zero matrix element between two levels  $i$  and  $j$  indicates a zero transition moment and hence a forbidden EPR transition. A non-zero element corresponds to an allowed or semi-allowed EPR transition. Whether the transitions are actually induced by a microwave pulse depends on the energy difference  $\omega_{ji} = \epsilon_j - \epsilon_i$ , the microwave frequency and the pulse length, which defines the excitation bandwidth of the pulse. Each matrix element is therefore multiplied by an excitation window function  $G(\Omega_S)$  that is maximum for on-resonance irradiation ( $\omega_{ji} = \omega_{mw}$ ) and zero if the microwave frequency is far off. The resulting matrix usually contains only two off-diagonal non-zero elements, between eigenstates  $i$  and  $j$ . In this case, the two levels  $i$  and  $j$  can be treated as an isolated two-level system, and pulse EPR signals can be simulated using the expectation values  $\langle i | S | i \rangle$  and  $\langle j | S | j \rangle$  and the nutation frequency  $\omega_{1,ij}$  of the transition given by

$$\omega_{1,ij} = 2\omega_1 |\langle i | x \cdot S | j \rangle| G(\omega_{ij} - \omega_{mw}). \quad (37)$$

When there are several transitions that are excited simultaneously, the formalism can still be applied as long as the transitions do not share a common level. The total signal is simply the sum over the signals from the isolated two-level systems.

In systems with  $S > 1/2$  with any magnitude of zero-field splitting, the assumption that transitions do not share a common level is not valid for a few isolated orientations of the spin system. For example, for an axial  $D$  tensor small compared to the electron Zeeman frequency, this happens when the angle between the applied magnetic field and the unique axis of the  $D$  tensor is around  $54^\circ$ . However, in a powder spectrum, these special orientations carry very little statistical weight and can be neglected.

It is straightforward to accommodate the effect of a nucleus with large hyperfine splitting (such as  $\text{Cu}^{2+}$ ,  $\text{Co}^{2+}$  or  $\text{Mn}^{2+}$  in corresponding mononuclear complexes) by simply including all relevant interactions of the nucleus into the Hamiltonian  $H_S$ . The nucleus affects the orientational and transition selectivity through the eigenvalues of  $H_S$ . It also slightly affects the frequencies of the ESEEM nuclei through influencing  $\langle i|S|i \rangle$ .<sup>61</sup>

### 4.3 Product rule

In the ideal-pulse limit, the echo modulation signal from a spin system with multiple nuclei can be expressed as a sum of products of signals from single nuclei. These so-called product rules are based on the factorization of the total nuclear subspace into individual nuclear subspaces and have been given for two-pulse ESEEM,<sup>18,20,21</sup> three-pulse ESEEM,<sup>24,62,63</sup> HYSORE<sup>42</sup> and the related 1D and 2D sum-combination peak experiments.<sup>43</sup> It is possible to derive a general form applicable to arbitrary pulse sequences.

In a spin system with several nuclei, the total nuclear sub-Hamiltonian for each electron spin manifold is the sum over the nuclear sub-Hamiltonians of all nuclei, e.g.  $H_x = H_{x1} + H_{x2} + \dots$ , since the nuclei do not interact, neither directly (the interaction is too small) nor indirectly (we have neglected the effect of the nuclei on energy levels in  $H_S$ ). As a consequence, the nuclear eigenvalues are simple sums,  $\varepsilon_x = \varepsilon_{x1} + \varepsilon_{x2}$ , and the nuclear eigenstates are tensor products  $M_x = M_{x1} \otimes M_{x2}$  and  $M_\beta = M_{\beta1} \otimes M_{\beta2}$ , so that we can factor the propagators from eqn (18)

$$A_t = e^{-iH_x t} = e^{-iH_{x1} t} \otimes e^{-iH_{x2} t} = A_1 \otimes A_2, \quad (38)$$

with a similar expression for  $B_t$ .

As we have shown, in the ideal-pulse limit each pathway contribution  $E^{(q)}$  to the total signal is the trace of a product,  $F_q$ , of  $A$  and  $B$  propagator matrices. Using the properties of the tensor product  $(C_1 \otimes C_2)(D_1 \otimes D_2) = (C_1 D_1) \otimes (C_2 D_2)$  and  $\text{tr}(C \otimes D) = \text{tr}(C)\text{tr}(D)$ , each pathway signal can be written as a single product of pathway signals from subsystems containing one nucleus each, e.g.,  $E^{(q)} = c_q \text{tr}(F_q) = c_q \text{tr}(F_{q1} \otimes F_{q2}) = c_q \text{tr}(F_{q1})\text{tr}(F_{q2})$ . Summing over all pathways contributing to the detected echo, we obtain the general product rule

$$E = \sum_q E^{(q)} = \sum_q c_q \prod_i \text{tr} F_{qi}, \quad (39)$$

where  $i$  indicates the nucleus and  $q$  indicates the pathway. For the most common ESEEM experiments, the echo amplitudes are

usually presented normalized to the amplitude  $E_0$  when all interpulse delays are zero,<sup>20–22</sup> where  $F_{qi} = \mathbb{1}$ . In the special case where all  $c_q$  are equal, this gives after a few algebraic manipulations the general normalized product rule

$$\tilde{E} = \frac{E}{E_0} = \frac{1}{n_p} \sum_q \prod_i \tilde{E}_i^{(q)}, \quad (40)$$

where  $n_p$  is the number of pathways. In essence, there is one product for each pathway contributing to the observed echo. The known product rules for two-pulse ESEEM (one product), three-pulse ESEEM (two products, prefactor 1/2) and HYSORE (two products, prefactor 1/2) follow directly from eqn (40), as do equivalent expressions for any other pulse sequence in the ideal-pulse limit.

The implications of eqn (40) for the ESEEM spectrum can easily be visualized if we recall the fact that a product in time domain corresponds to a convolution in frequency domain. A fundamental difference between ENDOR and ESEEM spectra of systems with many nuclei becomes apparent. Whereas the former are sums of single-nucleus spectra, the latter are convolutions thereof, featuring cross-nuclear combination lines, multi-quantum peaks, and inter-nuclear cross suppression.<sup>64,65</sup> Therefore it is necessary to include all deeply modulating nuclei in an ESEEM simulation, even when only other, weakly modulating nuclei are of interest. A procedure entirely analogous to the product rules above is an old method for the simulation of first-order cw EPR spectra of multinuclear spin systems using Fourier transformation.<sup>66</sup>

To apply the product rule to a given pulse sequence in a simulation, the time-domain signals due to the contributing pathways are computed in turn and then multiplied together. This has to be done separately for each orientation, frequency offset and/or EPR transition, and not only once at the end of a simulation. Therefore, when a frequency-domain method is used to construct the spectrum of a powder sample, many inverse Fourier transformations might be necessary, so that there are no time savings by using the product rule for two or three nuclei. Only with four or more nuclei it is advantageous to employ nuclear subspace factorization and the product rule. The time-domain evolution method is much slower in all cases. If pulses are not ideal, the product rule is not strictly applicable. Different pathways can have widely different electron coherence transfer amplitudes (analogous to  $c_q$  in the ideal-pulse limit), so that the assumption leading to eqn (40) is invalid. More importantly, the propagators of long pulses cannot generally be factorized, so that eqn (39) is also not applicable.<sup>50</sup> However, even if the product rule cannot or is not deployed, the nuclear subspace factorization can be used to speed up the diagonalization of the nuclear sub-Hamiltonians in eqn (4) prior to the computation of the pathway signals.

### 4.4 Pulse ENDOR

The simulation of the standard pulse ENDOR experiments based on polarization transfer<sup>1,48,49,67</sup> is possible through a straightforward extension of the theory presented above, first employed by Liao and Hartmann<sup>68</sup> for Mims ENDOR. In both Mims and Davies ENDOR experiments, the echo amplitude is observed as a function of the frequency  $\omega_{\text{rf}}$  of a

radiofrequency (rf) pulse. When this is not resonant with any nuclear transition, the echo is unaffected. When it is, the echo is reduced in intensity, as the rf pulse transfers nuclear polarization between sublevels so that the magnetization does not refocus completely at the time of the echo. In the case of Davies ENDOR, the echo is conventionally measured with negative phase, so that the measured ENDOR signal appears as a signal increase. The echoes in both Davies and Mims ENDOR are composed of the signals from two pathways, for which the signals can be written as

$$E^{(\alpha)}(\omega_{\text{rf}}) = \text{tr}[D_{\alpha}R(\omega_{\text{rf}})G_{\beta}R^{\dagger}(\omega_{\text{rf}})] \quad (41a)$$

$$E^{(\beta)}(\omega_{\text{rf}}) = \text{tr}[D_{\beta}R(\omega_{\text{rf}})G_{\alpha}R^{\dagger}(\omega_{\text{rf}})]. \quad (41b)$$

$G$  and  $D$  are the generator and detector submatrices that can be computed as discussed above.  $R(\omega_{\text{rf}})$  is a single-transition propagator matrix defined in the nuclear eigenbasis corresponding to an ideally selective rf pulse if the rf is resonant with a nuclear transition, or  $\mathbb{1}$  if off-resonant. The flip angle  $\theta_{\text{rf}}$  effected by  $R(\omega_{\text{rf}})$  depends on the matrix elements of  $I_x$  between the two sublevels of the resonant nuclear transition and on the hyperfine enhancement.<sup>48,69</sup> Any pulse ENDOR experiment with pathways of the structure in eqn (41) can be simulated by pre-computing  $G$  and  $D$  and then evaluating the expressions with  $R(\omega_{\text{rf}})$  for all values of  $\omega_{\text{rf}}$  that correspond to nuclear transition frequencies. For all other values,  $E = \text{tr}(DG)$ . With this approach, suppression effects due to non ideally selective pulses in Davies ENDOR<sup>70</sup> and the implicit TRIPLE effect in Mims ENDOR<sup>64</sup> can thus be accounted for.

## 5. Calculations

In the following, we show a few examples to illustrate some aspects of the formalism introduced above. All simulations were performed on a laptop computer (1.6 GHz Intel Pentium M, 1 GB RAM, Windows XP) running *EasySpin* 3.1 and *Matlab* 7.7 (The Mathworks Inc., Natick, MA).

### 5.1 High-electron spin, orientation selection

As described, the presence of anisotropic terms in  $H_S$  causes orientation and transition selection in a powder sample. At a given magnetic field, the microwave quantum  $\omega_{\text{mw}}$  is resonant with any of the EPR transitions for a small subset all possible orientations only. Such a situation can be easily handled, as is illustrated in Fig. 2 for the three-pulse ESEEM spectra of a single  $^1\text{H}$  nuclear spin ( $I = 1/2$ ) coupled to an  $S = 5/2$  electron spin with zero-field splitting of  $D = -100$  MHz. The top trace shows the full powder spectrum as a reference, simulated assuming (unrealistically) that the microwave pulses can simultaneously excite all  $|\Delta m_S| = 1$  EPR transitions spread over 800 MHz. The proton exhibits a resonance frequency that depends on the  $m_S$  manifold: the larger  $m_S$ , the larger the hyperfine contribution to the local field, which then adds or subtracts to the external field depending on the signs of  $m_S$ ,  $D$  and  $A$ . When the excitation width is narrowed to 50 MHz, it can be seen that not all five EPR transitions are excited, and correspondingly, fewer than six peaks appear in the spectrum. For example, at 362.0 mT (bottom trace), only the  $|3/2\rangle \leftrightarrow |5/2\rangle$  electron spin transition is resonant, and two

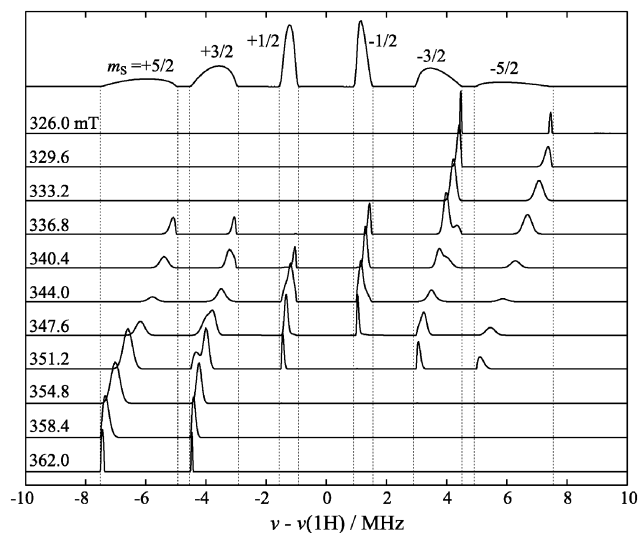


**Fig. 2** Simulation of the orientation and transition selectivity in three-pulse ESEEM of an  $S = 5/2$  system containing a proton. Parameters: 320 mT,  $g = 2$ ,  $D = -100$  MHz,  $A_{\perp} = 2$  MHz,  $A_{\parallel} = 3$  MHz.  $\tau = 0.1$  ns (blind-spot free),  $T$  incremented from 0 to 10.22  $\mu\text{s}$  (512 points). Ideal-pulse powder simulations with 50 MHz wide Gaussian excitation window and 901 orientations. Computation time: 0.2–1.1 s.

nuclear peaks from  $m_S = +5/2$  and  $m_S = +3/2$  are seen. The transition is resonant for a few orientations only, so that minor parts of the broad powder peaks are visible. The orientation selection is different for different EPR transitions, as can be seen from the two maxima in the  $m_S = +3/2$  region at 351.2 mT: one is due to the  $|3/2\rangle \leftrightarrow |5/2\rangle$  transition, and the other stems from  $|1/2\rangle \leftrightarrow |3/2\rangle$ , which is resonant for a different subset of orientations and has companion intensity in the  $m_S = +1/2$  region.

### 5.2 Many nuclear spins

Spectra from spin systems with many coupled nuclei often occur in applications, and the ability to simulate their pulse EPR spectra is indispensable for extracting structural information. With the theory developed in this work, they can be efficiently simulated.  $\text{Mn}(\text{imidazole})_6$  is such a complex system that has been studied with cw and pulse EPR. The magnetic parameters of the six octahedrally ligating imidazole nitrogens in this complex have recently been determined from HYSORE spectra of doped single crystals.<sup>10</sup> The  $3d^5$   $\text{Mn}^{2+}$  ion is high spin with  $S = 5/2$ , and the nucleus is 100% natural abundance  $^{55}\text{Mn}$  with  $I = 5/2$ . The nuclear spins  $I = 1$  of the six directly coordinating  $^{14}\text{N}$  atoms of the six imidazole ligands are detectable in HYSORE spectra at the Q-band (35 GHz, 1.2 T). A simulation of such a spectrum for one of the  $|1/2\rangle \leftrightarrow |3/2\rangle$  electron spin transitions is shown in Fig. 3. The corresponding experimental spectrum simulation is given in Fig. 6 in ref. 10. The spectrum contains many resolved peaks correlating fundamental single- and double-quantum as well as inter-nuclear combination frequencies. Due to its complexity, the spectrum cannot be analyzed manually, but its rich structure allows the spectroscopic parameters to be extracted by numerical simulation combined with automated

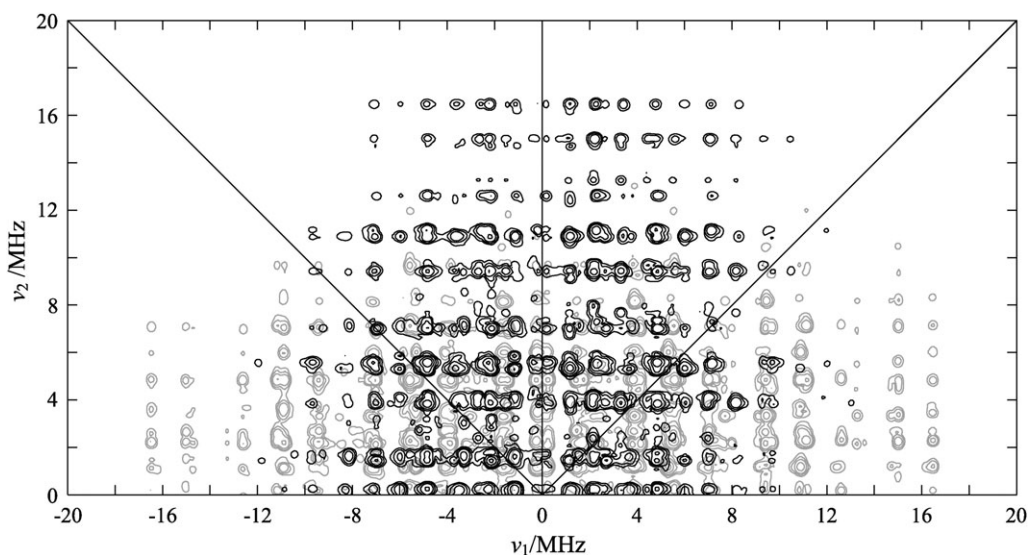


**Fig. 3** Simulation of the Q-band HYSCORE spectrum of a single orientation of  $\text{Mn}^{2+}$  (imidazole)<sub>6</sub>. The magnetic field is resonant with a  $|1/2\rangle \leftrightarrow |3/2\rangle$  electron spin transition. Spin parameters:  $g = 2.0036$ ,  $A(\text{Mn}) = -259$  MHz,  $D = -318$  MHz,  $E = -51$  MHz with Euler angles  $\alpha = 100^\circ$ ,  $\beta = 23^\circ$ ,  $\gamma = 0^\circ$ , hyperfine principal values  $A(\text{N}1) = A(\text{N}4) = (2.50, 2.62, 4.45)$  MHz,  $A(\text{N}2) = A(\text{N}5) = (4.37, 2.65, 2.64)$  MHz,  $A(\text{N}3) = A(\text{N}6) = (2.75, 4.40, 2.60)$  MHz, quadrupole principal values  $Q(\text{N}1) = Q(\text{N}4) = (0.7, 0.8, -1.5)$  MHz,  $Q(\text{N}2) = Q(\text{N}5) = (-1.5, 0.5, 1.0)$  MHz,  $Q(\text{N}3) = Q(\text{N}6) = (0.8, -1.5, 0.7)$  MHz. Experimental parameters: magnetic field 1251 mT along  $z$  axis of  $D$  tensor,  $\tau = 208$  ns,  $t_1$  and  $t_2$  incremented from 0 to 5.1  $\mu\text{s}$  in steps of 20 ns (256 points), ideal pulses, product rule. Contour levels at 2.5, 5, 10, 25 and 50% of maximum. Gray:  $(|3/2\rangle, |1/2\rangle)$  correlations, black:  $(|1/2\rangle, |3/2\rangle)$  correlations. Computation time: 6.1 s.

fitting. There are slight differences in peak intensities between the simulated and the experimental spectrum, with the simulated spectrum featuring more intense peaks than the experimental spectrum. Altogether however, the correspondence is surprisingly good, showing that the theory developed in this work is valid and can help analyze spectra from quite large spin systems.

### 5.3 Non-ideal pulses

Non-ideal pulses are included in the present framework. As an example, we look at matched HYSCORE,<sup>51</sup> where the second and fourth pulse of a standard HYSCORE sequence are replaced by long non-ideal pulses with high nominal turning angles. The lengths are chosen such that the second pulse maximizes the generation of single- or multi-quantum nuclear coherence from allowed electron coherence, and the fourth pulse maximizes the reverse transfer back to allowed electron coherence that can be detected. Experimentally, the lengths of these matched pulses are varied until optimum signal intensity is found.

With simulations, suitable pulse lengths can be explored in advance. This is illustrated in Fig. 4 for two protons coupled to an electron spin  $S = 1/2$ . When all pulses have their standard flip angles, only correlations peaks between single-quantum (sq) frequencies of the protons are visible. As the lengths and thus the nominal flip angles of the second and the fourth pulse are increased, double-quantum (dq) coherences are increasingly generated and detected. A dq-dq correlation ridge crosses the diagonal, whereas two sq-dq ridges appear above and below the diagonal. The presence and the positions of these multi-quantum peaks help determine the number of nuclei and the relative signs of their interaction tensors. With simulations like this, the optimal pulse length for the detection of multi-quantum peaks can be determined.

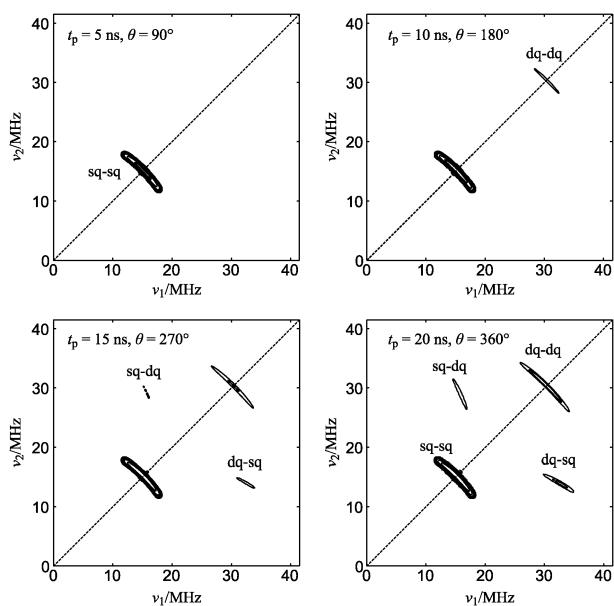


**Fig. 4** Simulations of the effect of pulse lengths on a matched HYSCORE spectrum. Sequence:  $(90^\circ, 5 \text{ ns})_x - \tau - (\theta, t_p) - t_1 - (180^\circ, 5 \text{ ns}) - t_2 - (\theta, t_p) - \tau$ , where  $t_p$  is the pulse length and  $\theta$  the nominal flip angle of the second and the fourth pulses. Parameters:  $S = 1/2$ ,  $g = 2$ , two equivalent  $^1\text{H}$  with  $A_\perp = -6$  MHz,  $A = 6$  MHz;  $\tau = 100$  ns, 350 mT,  $t_1$  and  $t_2$  incremented from 0 to 3.06  $\mu\text{s}$  in 12-ns steps (256 points). Powder simulation with 91 orientations, 21-point offset integration. Contour levels at 0.25, 0.5, 1, 2.5, 5, 10, 25 and 50% of maximum. Computation time: 17 s each.

### 5.4 Pulse ENDOR

The fact that the formalism can be applied as described to pulse ENDOR is illustrated in Fig. 5 with exemplary

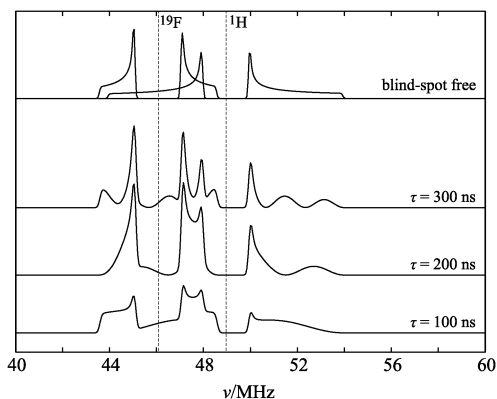


**Fig. 5** Simulation of Mims ENDOR spectra for a  $S = 1/2$  electron spin coupled to both a  $^1\text{H}$  and a  $^{19}\text{F}$  nucleus. Parameters:  $A(^1\text{H}) = (2,2,10)$  MHz,  $A(^{19}\text{F}) = (2,2,5)$  MHz, 1150 mT, powder simulations with ideal pulses. Computation times: 0.1 s per spectrum.

simulations of Mims ENDOR at 35 GHz and 1150 mT of a spin system containing two nuclei,  $^1\text{H}$  and  $^{19}\text{F}$ . Each gives rise to two ENDOR peaks, centered at their respective Larmor frequencies, 49.0 and 46.1 MHz, shown in the top trace. Mims ENDOR spectra exhibit  $\tau$ -dependent suppression effects that modify these theoretical lineshapes. The intensity of all peaks is modulated with an envelope of  $\sin^2(A\tau/2)$ , where  $A$  is the hyperfine coupling for a given nucleus and orientation of the spin system in angular frequencies.<sup>48</sup> The spectra for three different  $\tau$  values are shown in the lower traces. For  $\tau = 100$  ns, the  $^{19}\text{F}$  peaks are fairly undistorted, but the envelope of the two  $^1\text{H}$  peaks is severely distorted by the  $\tau$  suppression, so that the singularity at 50 MHz is greatly reduced in intensity. At  $\tau = 200$  ns, also the  $^{19}\text{F}$  peaks are strongly affected. When  $\tau$  reaches 300 ns, the entire spectrum is scattered with blindspots.

## 6. Conclusions and outlook

The theory outlined above introduces a general approach to simulate spectra obtained from electron spin echo experiments. It is based on the common and widely valid assumption that only one or non-adjacent EPR transitions are excited in the experiment. The method automatically analyzes any given pulse experiment consisting of a sequence of microwave pulses with fixed and incremented inter-pulse delays to determine the electron coherence transfer pathways that contribute to the observed echo of interest. For these pathways, explicit expressions for the signal contributions are automatically written down. The signal is constructed by using an improved variation of the frequency-domain histogram method. All the theory of this paper is implemented in *EasySpin*<sup>7</sup> and is accessible *via* a simple user interface.

The method presented here contains new theoretical elements that make it more general than existing approaches in several respects: (1) it is not limited to specific pulse experiments. Scalar expressions for even the most complicated pulse experiments are automatically derived. (2) High electron spin systems are easily accommodated in a very general way,

without the necessity of neglecting nonsecular terms. Also, nuclei can be included that affect the EPR resonance fields, but are undetectable in ESEEM. (3) The method is applicable to many nuclei, with any size and orientation of the nuclear quadrupole tensor compared to their hyperfine tensor. (4) Spectra from pulse ENDOR experiments based on polarization transfer can be simulated. (5) Non-ideal pulses are treated in the same framework, making it possible to simulate experiments with selective or matched pulses. (6) A general product rule for arbitrary sequences has been derived in order to accelerate simulations with systems containing many nuclei. (7) The method used to construct the spectrum from the trace expressions is more efficient than time domain calculations and more accurate than frequency-domain histogram techniques.

The theory does not cover every possible pulse EPR experiment. In the form and scope presented above, it is not directly applicable to time-domain pulse ENDOR, experiments with field jumps during the pulse sequence, or experiments involving multiple microwave frequencies such as double electron-electron resonance (DEER). The theory does not accommodate the detection of free induction decays or the use of boxcar detection.<sup>71</sup> Also, shaped pulses and chirp pulses were not implemented. However, the theory for these types of pulses is essentially known and amounts only to the computation of additional propagators, so that they should easily be accommodated within the framework.

With the approach presented in this work, automatic least-squares fitting can be applied to a wide range of pulse EPR experiments. Such fitting methods have not been widely applied yet in pulse EPR, and it is currently not clear which algorithms and which error function will yield the best results. For cw EPR, hybrid methods are considered most efficient. They combine a global search algorithm (*e.g.* genetic) that determines regions of potential minima in parameter space with a local algorithm (*e.g.* simplex or Levenberg–Marquardt) that determines the minima in these regions. These methods are also applicable to pulse EPR, and preliminary explorations suggest that they perform similarly. Another important factor affecting the robustness and effectiveness of automatic fitting procedures is the choice of  $y$  in the computation of the sum-of-squares objective function from experimental and simulated data,  $\sum_k (y_{\text{exp},k} - y_{\text{sim},k})^2$ . In cw EPR,  $y$  can be the spectrum, its integral, its double integral, or its Fourier transform. The double integral has the advantage that it is a monotonic function of the abscissa and that the number of local minima in parameter space is therefore minimized. In pulse EPR, the same method can be applied to frequency-domain data (ENDOR or Fourier transform of ESEEM time-domain), whereas in time-domain a direct fit to the experimental data seems to be most robust. Also, ESEEM fitting in the time domain has the advantage that the fitting error can be assessed more directly.

## Acknowledgements

We thank Troy A. Stich for valuable discussions and for carefully reading the manuscript. This work was supported by NIH grant GM48242.

## References

- 1 A. Schweiger and G. Jeschke, *Principles of Pulse Electron Paramagnetic Resonance*, Oxford University Press, Oxford, 2001.
- 2 Y. Deligiannakis, M. Louloudi and N. Hadjiliadis, *Coord. Chem. Rev.*, 2000, **204**, 1–112.
- 3 T. Prisner, M. Rohrer and F. MacMillan, *Annu. Rev. Phys. Chem.*, 2001, **52**, 279–313.
- 4 S. Van Doorslaer and E. Vinck, *Phys. Chem. Chem. Phys.*, 2007, **9**, 4620–4638.
- 5 G. R. Hanson, K. E. Gates, C. J. Noble, M. Griffin, A. Mitchell and S. Benson, *J. Inorg. Biochem.*, 2004, **98**, 903–916.
- 6 S. Stoll and A. Schweiger, *Chem. Phys. Lett.*, 2003, **380**, 464–470.
- 7 S. Stoll and A. Schweiger, *J. Magn. Reson.*, 2006, **178**, 42–55.
- 8 S. Stoll and A. Schweiger, *Biol. Magn. Reson.*, 2007, **27**, 299–321.
- 9 E. Vinck and S. Van Doorslaer, *Phys. Chem. Chem. Phys.*, 2004, **6**, 5324–5330.
- 10 I. García-Rubio, A. Angerhofer and A. Schweiger, *J. Magn. Reson.*, 2007, **184**, 130–142.
- 11 J. J. Shane, *PhD thesis*, University of Nijmegen, 1993.
- 12 R. Szoszenfogel and D. Goldfarb, *Mol. Phys.*, 1998, **95**, 1295–1308.
- 13 J. J. Shane, L. P. Liesum and A. Schweiger, *J. Magn. Reson.*, 1998, **134**, 72–75.
- 14 Z. Mádi, S. Van Doorslaer and A. Schweiger, *J. Magn. Reson.*, 2002, **154**, 181–191.
- 15 A. V. Astashkin and A. M. Raitsimring, *J. Chem. Phys.*, 2002, **117**, 6121–6132.
- 16 G. R. Hanson, C. J. Noble and S. Benson, *Biol. Magn. Reson.*, 2009, **28**, 105–174.
- 17 L. Sun, J. Hernandez-Guzman and K. Warncke, *J. Magn. Reson.*, DOI: 10.1016/j.jmr.2009.05.012.
- 18 L. G. Rowan, E. L. Hahn and W. B. Mims, *Phys. Rev.*, 1965, **137**, A61–A71.
- 19 G. M. Zhidomirov and K. M. Salikhov, *Teor. Eksp. Khim.*, 1968, **4**, 514–519 (*Theor. Exp. Chem.*, 1971, **4**, 332–334).
- 20 D. Grischkowsky and S. R. Hartmann, *Phys. Rev. B: Condens. Matter Mater. Phys.*, 1970, **2**, 60–74.
- 21 W. B. Mims, *Phys. Rev. B: Condens. Matter Mater. Phys.*, 1972, **5**, 2409–2419.
- 22 W. B. Mims, *Phys. Rev. B: Condens. Matter Mater. Phys.*, 1972, **6**, 3543.
- 23 W. B. Mims, in *Electron Paramagnetic Resonance*, ed. S. Geschwind, Plenum Press, New York, 1972, pp. 263–351.
- 24 S. A. Dikanov, A. A. Shubin and V. N. Parmon, *J. Magn. Reson.*, 1981, **42**, 474–487.
- 25 C. Gemperle and A. Schweiger, *J. Magn. Reson.*, 1990, **88**, 241–256.
- 26 J. J. Shane, P. Höfer, E. J. Reijerse and E. de Boer, *J. Magn. Reson.*, 1992, **99**, 596–604.
- 27 S. Stoll and A. Schweiger, *J. Magn. Reson.*, 2003, **163**, 248–256.
- 28 W. B. Mims, J. Peisach and J. L. Davies, *J. Chem. Phys.*, 1977, **66**, 5536–5550.
- 29 C. P. Keijzers, E. J. Reijerse, P. Stam, M. F. Dumont and M. C. M. Gribnau, *J. Chem. Soc., Faraday Trans. 1*, 1987, **83**, 3493–3503.
- 30 E. J. Reijerse and C. P. Keijzers, *J. Magn. Reson.*, 1987, **71**, 83–96.
- 31 R. G. Larsen, C. J. Halkides and D. J. Singel, *J. Chem. Phys.*, 1993, **98**, 6704–6721.
- 32 L. G. Rowan, *J. Magn. Reson.*, 1987, **74**, 308–315.
- 33 G. M. Muha, *J. Chem. Phys.*, 1980, **73**, 4139–4140.
- 34 G. M. Muha, *J. Magn. Reson.*, 1983, **53**, 85–102.
- 35 A. V. Astashkin, S. A. Dikanov and Yu. D. Tsvetkov, *J. Struct. Chem.*, 1984, **25**, 45–55.
- 36 H. L. Flanagan and D. J. Singel, *J. Chem. Phys.*, 1987, **87**, 5606–5616.
- 37 M. T. Bennebroek and J. Schmidt, *J. Magn. Reson.*, 1997, **128**, 199–306.
- 38 B. Epel, A. Pöpl, P. Manikandan, S. Vega and D. Goldfarb, *J. Magn. Reson.*, 2001, **148**, 388–397.
- 39 J. J. L. Morton, N. S. Lees, B. M. Hoffman and S. Stoll, *J. Magn. Reson.*, 2008, **191**, 315–321.
- 40 N. P. Benetis, P. C. Dave and D. Goldfarb, *J. Magn. Reson.*, 2002, **158**, 126–142.
- 41 S. Stoll and B. Kasumaj, *Appl. Magn. Reson.*, 2008, **35**, 15–32.
- 42 A. M. Tyryshkin, S. A. Dikanov and D. Goldfarb, *J. Magn. Reson. A*, 1993, **105**, 271–283.
- 43 S. Van Doorslaer and A. Schweiger, *Chem. Phys. Lett.*, 1997, **281**, 297–305.
- 44 M. Hubrich, G. Jeschke and A. Schweiger, *J. Chem. Phys.*, 1996, **104**, 2172–2184.
- 45 D. Goldfarb, V. Kofman, J. Libman, A. Shanzer, R. Rahmatouline, S. Van Doorslaer and A. Schweiger, *J. Am. Chem. Soc.*, 1998, **120**, 7020–7029.
- 46 A. V. Astashkin and A. M. Raitsimring, *J. Magn. Reson.*, 2000, **143**, 280–291.
- 47 D. Wang and G. R. Hanson, *J. Magn. Reson. A*, 1995, **177**, 1–8.
- 48 C. Gemperle and A. Schweiger, *Chem. Rev.*, 1991, **91**, 1481–1505.
- 49 H. Thomann and M. Bernardo, *Methods Enzymol.*, 1993, **227**, 118–189.
- 50 G. Jeschke and A. Schweiger, *J. Chem. Phys.*, 1996, **105**, 2199–2211.
- 51 G. Jeschke, R. Rakhmatullin and A. Schweiger, *J. Magn. Reson.*, 1998, **131**, 261–271.
- 52 L. Liesum and A. Schweiger, *J. Chem. Phys.*, 2001, **114**, 9478–9488.
- 53 D. J. Sloop, H.-L. Yu, T.-S. Lin and S. I. Weissman, *J. Chem. Phys.*, 1981, **75**, 3746–3757.
- 54 T. S. Lin, *Chem. Rev.*, 1984, **84**, 1–15.
- 55 D. J. Singel, W. A. J. A. van der Poel, J. Schmidt, J. H. van der Waals and R. de Beer, *J. Chem. Phys.*, 1984, **81**, 5453–5461.
- 56 A. R. Coffino and J. Peisach, *J. Chem. Phys.*, 1992, **97**, 3072–3091.
- 57 P. B. Oliete, V. M. Orera and P. J. Alonso, *Phys. Rev. B: Condens. Matter Mater. Phys.*, 1996, **54**, 12099–12108.
- 58 X. Tan, M. Bernardo, H. Thomann and C. P. Scholes, *J. Chem. Phys.*, 1993, **98**, 5147–5157.
- 59 B. E. Sturgeon, J. A. Ball, D. W. Randall and R. D. Britt, *J. Phys. Chem.*, 1994, **98**, 12871–12883.
- 60 R. Vardi, M. Bernardo, H. Thomann, K. G. Strohmaier, D. E. W. Vaughan and D. Goldfarb, *J. Magn. Reson.*, 1997, **126**, 229–241.
- 61 M. Iwasaki, *J. Magn. Reson.*, 1974, **16**, 417–423.
- 62 S. A. Dikanov, V. F. Yudanov and Yu. D. Tsvetkov, *J. Magn. Reson.*, 1979, **34**, 631–645.
- 63 S. A. Dikanov and Y. D. Tsvetkov, *Electron Spin Echo Envelope Modulation (ESEEM) Spectroscopy*, CRC Press, Boca Raton, 1992.
- 64 P. Doan, M. J. Nelson, H. Jin and B. M. Hoffman, *J. Am. Chem. Soc.*, 1996, **118**, 7014–7015.
- 65 S. Stoll, C. Calle, G. Mitrikas and A. Schweiger, *J. Magn. Reson.*, 2005, **177**, 93–101.
- 66 J. C. Evans, P. H. Morgan and R. H. Renaud, *Anal. Chim. Acta*, 1978, **103**, 175–187.
- 67 A. Grupp and M. Mehring, in *Modern Pulsed and Continuous-Wave Electron Spin Resonance*, ed. L. Kevan and M. K. Bowman, Wiley, New York, 1990, pp. 195–229.
- 68 P. F. Liao and S. R. Hartmann, *Phys. Rev. B: Condens. Matter Mater. Phys.*, 1973, **8**, 69–80.
- 69 L. R. Dalton and A. L. Kwiram, *J. Chem. Phys.*, 1972, **57**, 1132–1145.
- 70 C. Fan, P. E. Doan, C. E. Davoust and B. M. Hoffman, *J. Magn. Reson.*, 1992, **98**, 62–72.
- 71 C. Gemperle, A. Schweiger and R. R. Ernst, *J. Magn. Reson.*, 1991, **91**, 273–288.